Contrast Enhancement of Spectral Domain Optical Coherence Tomography Using Spectrum Correction

Guangming Ni,[1, 2] Linbo Liu,[2, *] Xiaojun Yu,[2, 3] Xin Ge,[2] Si Chen,[2] Xinyu Liu,[2] Xianghong Wang,[2] Shi Chen[2]

[1]*State Key Laboratory of Electronic Thin Films and Integrated Devices, School of Optoelectronic Information, University of Electronic Science and Technology of China, No. 4, Section 2, North Jianshe Road, Chengdu, China, 610054*

[2]*School of Electrical and Electronic Engineering, Nanyang Technological University, Singapore, 639798*

[3]*School of Automation, Northwestern Polytechnical University, Xi'an, Shaanxi, China, 710072*

ARTICLEINFO

Keywords:
Optical coherence tomography;
Biophotonics;
Spectrum correction

ABSTRACT

We report a spectrum correction method to enhance the image contrast of spectral domain optical coherence tomography (SD-OCT). Our method treats SD-OCT signals as the product of harmonic signals backscattered from a sample comprising a series of discrete reflectors and a window corresponding to the light source spectrum. The method restores the magnitude of the main lobe of the axial point spread function (PSF) by estimating the magnitudes of the backscattered harmonic signals and strengthens OCT signals using these estimated values. Experimental results acquired from fresh rat corneas and fixed human aortic atherosclerosis tissues show that our method provides clearer microstructural information than the conventional methods by improving the contrast to noise ratios (CNRs) by 1.4779 dB and 3.2595 dB, respectively. This improved image quality is obtained without any hardware change, making our method a cost-effective alternative to compete with hardware advances.

Introduction

Optical coherence tomography (OCT) is a powerful non-invasive imaging tool that is widely used for three-dimensional imaging of biological tissue[1-3]. By measuring the magnitude and echo time delay of backscattered light using a low coherence light source, OCT can provide high-resolution images of the microstructure of biological tissue[4-7]. Therefore, it has become one of the most widely used imaging tools for disease diagnoses[6, 8-10]. Improving image quality can be achieved by improving the axial resolution and contrast in both biomedical and industrial applications. Many works have been dedicated to improving OCT image quality by contrast enhancement methods using hardware or software-based methods. For example, better quality images have been obtained using exogenous contrast agents, such as gold nanoparticles, nanorods, and microspheres[11-15]. However, these methods confer higher hardware costs, are inconvenient to operate and have poor applicability. Software-based methods for OCT image contrast enhancement can be categorized into A-scan and B-scan based methods. Typically, A-scan based methods perform spectroscopic analysis to add new contrast such as particle size to images [16]. Nevertheless, previous A-scan based methods are computationally costly. The B-scan based methods, such as

*Corresponding author: LIULINBO@ntu.edu.sg

statistical modeling[17], histogram matching[18], multiple B-scan averaging[19], image fusion[20] and adaptive compensation[21, 22], also improved OCT images of the retina, the optic nerve head, the lamina cribrosa, etc. However, B-scan based methods always can't deal with the contrast reduction caused by sidelobe artifacts well and clean the signal, especially for micro OCT (μOCT) with spatial resolution of 1-2 um [23-25].

OCT interference signals can be regarded as the product of harmonic signals backscattered from a sample comprising a series of discrete reflectors and a window corresponding to the light source spectrum. When using fast Fourier transform (FFT) to process SD-OCT spectral interference fringes, the FFT result is the convolution of the Fourier transforms of the light source spectrum and the backscattered harmonic signals. Windowing these backscattered harmonic signals using the light source spectrum broadens their main lobe and introduces sidelobe artifacts, which degrades OCT image resolution and contrast. Spectral shaping techniques have been thoroughly investigated to reduce sidelobe artifacts in axial PSF for non-Gaussian-shaped laser source spectra[26]. However, these methods might broaden the main lobe and detailed information of tissue microstructures maybe therefore lost.

In this paper, we report a spectrum correction method to enhance SD-OCT image contrast, from a new perspective of digital signal processing. By strengthening OCT signals through estimating the amplitudes of backscattered harmonic signals and restoring the amplitudes of the main lobe of the axial PSF with the estimated values, this method suppresses sidelobe artifacts and enhances SD-OCT image contrast. We preformed imaging experiments on fresh rat corneas and fixed human aortic atherosclerosis tissues to demonstrate the advantages of our method over the existing methods.

1. Methods

1.1 Fundamental Methods

For a harmonic signal $B\cos(z_0 t)$, where t is a variable, z_0 and B are constants, the main lobe of its Fourier transform is $B\delta(z \pm z_0)$, which has a nonzero value B at $\pm z_0$ without any sidelobes. However, when it is multiplied by a window, windowing enlarges the full width at half maximum (FWHM) of its main lobe, reduces its main lobe amplitude and introduces sidelobe artifacts. In SD-OCT imaging, the interferometric signal can be expressed as $i_{OCT}(k)$, shown in Eq. 1,

$$\begin{aligned} i_{OCT}(k) &= \frac{\rho}{2}\sum_{j=1}^{M}[s(k)\cdot\sqrt{R_R R_{Sj}}(\cos[2k(z_R - z_{Sj})]] \\ &= s(k)\cdot d(k) \end{aligned} \tag{1}$$

where R_R and R_{Sj} are the backscattering indices of the reference arm and the sample interfaces, k is the wavenumber, $s(k)$ is the spectrum of the light source, M is the number of interfaces in the sample between layers of different refractive indices, z_R and z_{Sj} are the axial positions of the reference reflector and $j-th$ interface in the sample, ρ is the responsivity of the detector, and $d(k) = \frac{\rho}{2}\sum_{j=1}^{M}\sqrt{R_R R_{Sj}}(\cos[2k(z_R - z_{Sj})]$, which is the finite accumulation signal of the backscattered harmonic signals.

When OCT images are obtained using the Fourier transform $I_{OCT}(z)$ of $i_{OCT}(k)$, $I_{OCT}(z)$ can be expressed as Eq. 2,

$$I_{OCT}(z) = FFT[i_{OCT}(k)] = S(z) * D(z) \tag{2}$$

where z is the thickness position, $D(z) = \sum_{j=1}^{M}\frac{\rho}{4}\sqrt{R_R R_{Sj}}\delta[z \pm 2(z_R - z_{Sj})]$ is the Fourier transform of $d(k)$, $\delta(z \pm 2(z_R - z_{Sj}))$ is the Dirac delta function, and $S(z)$ is the Fourier transform of $s(k)$.

In Eq. 1, $i_{OCT}(k)$ can be regarded as the windowed result of $d(k)$ using $s(k)$ (here, we regard $s(k)$ and $d(k)$ as the window and the signal, respectively), and thus $I_{OCT}(z)$ is the convolution between $S(z)$ and $D(z)$, as shown in Eq. 2. The main lobe of the Fourier transform of each harmonic signal in $d(k)$ is shown in Fig.1(c), and its amplitude is lower than A because the convolution between the Fourier transform of the harmonic signal and the sampling window has a smoothing effect and reduces the main lobe amplitude, but we can use the spectrum correction method to obtain the amplitude $A=\frac{\rho}{2}\sqrt{R_R R_{Sj}}$ [27].

The fundamental idea of the method proposed in this paper is to first reshape the light source to a Hann spectral source and then obtain the main lobe amplitude of $D(z)$ to replace the main lobe amplitude of $I_{OCT}(z)$. The spectrum correction method is used to strengthen the coherence amplitude in the main lobe of the axial PSF in SD-OCT imaging and to achieve better contrast performance. As shown in Fig. 1(b), we first multiply SD-OCT signal data $i_{OCT}(k)$ by the spectral reshaping function $w(n)$ to reshape the light source to a Hann spectral source which has a better balance between the axial resolution and the sidelobes, as expressed by Eq. 3.

$$\begin{aligned} i'_{OCT}(k) &= w(k)\cdot i_{OCT}(k) \\ &= \frac{\rho}{2}\sum_{j=1}^{M}[[w(k)\cdot s(k)]\cdot\sqrt{R_R R_{Sj}}(\cos[2k(z_R - z_{Sj})]] \\ &= s'(k)\cdot d(k) \end{aligned} \quad (3)$$

In Eq. 3, $w(n)$ is the spectral reshaping window, which is defined by the ratio of this ideal Hann source spectrum and the measured spectral density using the spectral reshaping method[26], n is the serial number index of the reshaping function sequence, N is the pixel number of the A-scan signal, $s'(k)=w(k)\cdot s(k)$ is the spectral reshaping light source, and $S'(z)$ is the Fourier transform of $s'(k)$, as given in Eq. 4,

$$S'(z)=\frac{\sin(\pi z)}{\pi z}\frac{0.5z^2}{1-z^2} \quad (4)$$

When windowing a harmonic signal $A(\cos[2k(z_R - z_{Sj})]$ using $s'(k)$, we obtain the new windowed signal $s'(k)\cdot A(\cos[2k(z_R - z_{Sj})]$. The windowed signal's amplitude is lower than the harmonic signal because windowing broadens the main lobe of the harmonic signal's power spectrum and reduces the main lobe amplitude, but we can use spectrum correction technology to estimate A from the windowed signal[27]. Hence, we further use the spectrum correction method to estimate the amplitude of each harmonic signal in $d(k)$ to restore the main lobe amplitude in the Fourier transform $I'_{OCT}(z)$ of $i'_{OCT}(k)$ to enhance image contrast.

With Eq. 4, we can obtain Eq. 5 and Eq. 6 as below, where m is the serial-number index in the main lobe of discrete calculation sampling values of the Fourier transform of $s'(k)\cdot A(\cos[2k(z_R - z_{Sj})])$, as shown in Fig. 1(b), $y(z-z_0)$ is the amplitude function of the main lobe of Fourier transform of $s'(k)\cdot A(\cos[2k(z_R - z_{Sj})])$, z_0 is the abscissa centroid of the main lobe and Δz is the axial resolution of the SD-OCT imaging system.

$$\begin{aligned} &(m-1)S'(m)+(m+2)S'(m+1) \\ &=(m-1)\frac{\sin(\pi m)}{\pi m}\frac{0.5}{1-m^2}+ \\ &(m+2)\frac{\sin(\pi(m+1))}{\pi(m+1)}\frac{0.5}{1-(m+1)^2}=0 \end{aligned} \quad (5)$$

$$y(z-z_0)=A\frac{\sin(\pi(z-z_0))}{\pi(z-z_0)}\frac{0.5}{1-(z-z_0)^2} \quad (6)$$

Second, according to the barycenter method, the abscissa centroid z_0 of the main lobe can be obtained by using two adjacent serial-number indices m and $m+1$ in the main lobe with the highest amplitudes, as shown in Fig. 1(b). The obtained z_0 is expressed in Eq. 7[27].

$$z_0 = \frac{(m-1)\,y_m - (m+2)\,y_{m+1}}{y_m + y_{m+1}}\Delta z = m\Delta z + \frac{2\,y_{m+1} - y_m}{y_m + y_{m+1}}\Delta z \qquad (7)$$

From Eq. 7, we can obtain the axial error Δz_0 between the max's abscissa and the main lobe abscissa centroid z_0, as shown in Eq. 8, which considers the situation that serial-number index $m-1$ is the sub-max, as shown in Fig.1[27].

$$\Delta z_0 = (z_0 - m\Delta z) = \begin{Bmatrix} (\frac{2\,y_{m+1} - y_m}{y_m + y_{m+1}})\Delta z, y_{m+1} > y_{m-1} \\ (\frac{y_m - 2\,y_{m-1}}{y_m + y_{m-1}})\Delta z, y_{m-1} > y_{m+1} \end{Bmatrix} \qquad (8)$$

As shown in Fig. 1(b), because $y_m = y(z - z_0) = y(m\Delta z - z_0)$, we can obtain the amplitude A of the harmonic signal $A(\cos[2k(z_R - z_{Sj})]$ from $d(k)$ using Eq. 10 which can be obtained from Eq. 7 and Eq. 9.

$$y(z - z_0) = y_m = A \cdot S'(\Delta z_0) = A \cdot \frac{\sin(\pi\Delta z_0)}{\pi\Delta z_0} \cdot \frac{0.5\Delta z_0^{\,2}}{1 - \Delta z_0^{\,2}} \qquad (9)$$

$$A = \frac{y_m}{S'(\Delta z_0)} = y_m \cdot \frac{\pi\Delta z_0}{\sin(\pi\Delta z_0)} \cdot \frac{1 - \Delta z_0^{\,2}}{0.5\Delta z_0^{\,2}} \qquad (10)$$

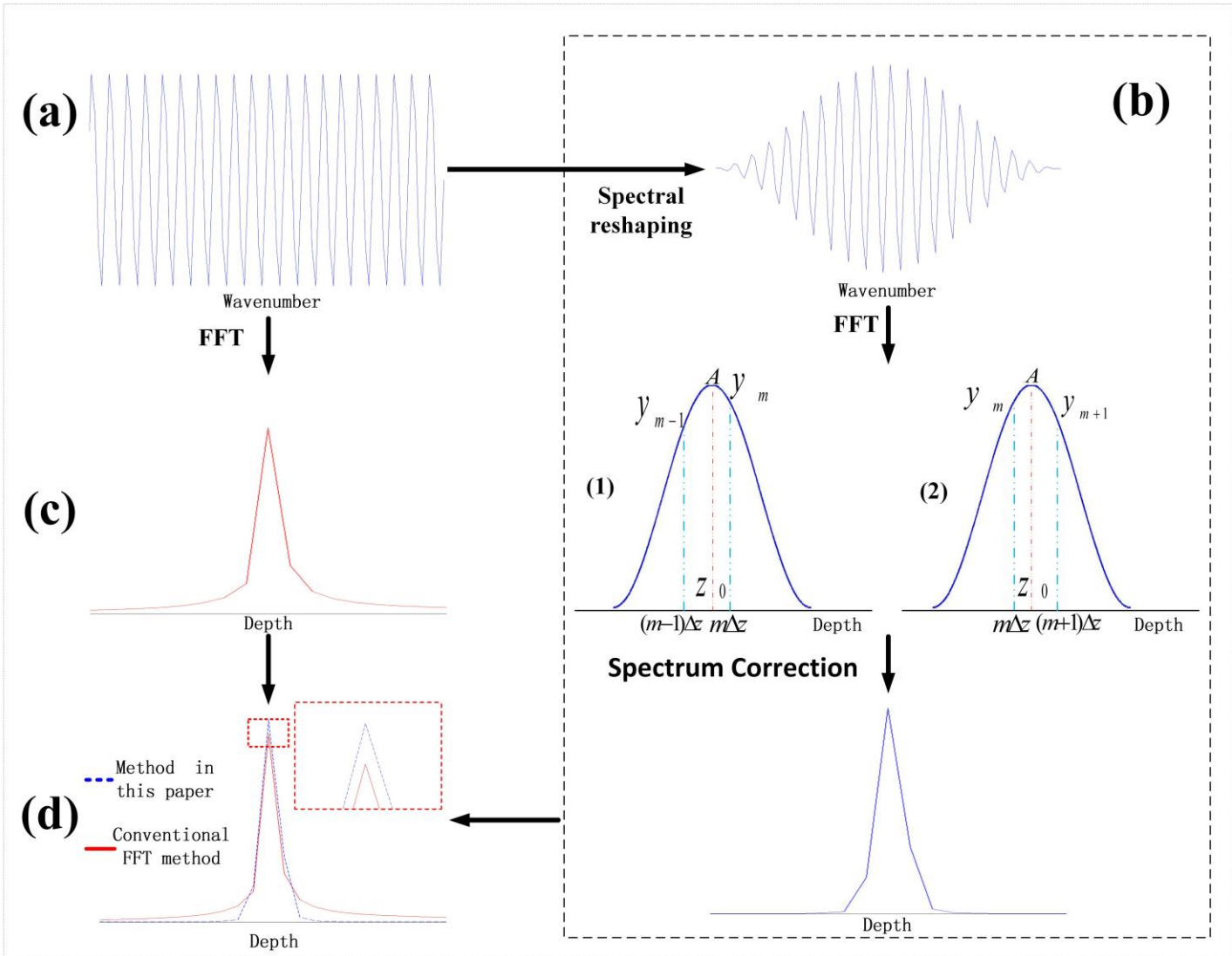

Fig. 1. Principles of the conventional FFT method and the method proposed in this paper, and the difference in the results between them. (a) Interferogram signal sampled from an OCT signal by a line scan camera (after removing constant terms from the signal). (b) The method in this paper using the spectrum correction method retrieves the depth profiles from the interferogram signal, including spectral reshaping, takes the Fourier transform, and finally performs spectrum correction to obtain the final data, where A is the theoretical value, and y_m , y_{m-1} and y_{m+1} are the values calculated from the interferogram signal. (1) the max y_m is in front of the sub max y_{m-1} in a main lobe, (2) the max y_m is behind the sub max y_{m+1} in a main lobe. (c) Conventional FFT method using Fourier transform to retrieve depth profiles from the interferograms. (d) Difference in the results between the conventional FFT method and the method proposed in this paper.

Here we list the processing steps of the proposed spectrum correction method as follows,

Step 1. Load the original imaging data to perform the linearity correction and dispersion correction, and

obtain a new data set.

Step 2. Obtain A-scan data $i_{OCT}(n), n = 1,2,\cdots,N$ from the obtained new data set, where n is the A-line index of an A-scan signal sequence, and N is the pixel number of the line camera used in the SD-OCT system.

Step 3. Obtain the new A-scan data $i'_{OCT}(n), n = 1,2,\cdots,N$ by multiplying $i_{OCT}(n)$ by the spectral reshaping function $w(n)$. This step can reshape the light source spectrum using a digital method, which is the basis of Step 5, and can also suppress sidelobe artifacts.

Step 4. Perform FFT of $i'_{OCT}(n)$ and obtain its Fourier transform $I'_{OCT}(n) = abs(FFT(i'_{OCT}))$.

Step 5. Perform spectrum correction. This step can further enhance the image contrast.

5-1. Search the peaks $P(l)$ in each main lobe in $I'_{OCT}(n)$, where l is the serial-number index of the local maximum sequence in $I'_{OCT}(n)$.

5-2. Search the sub-peak $P'(l)$ in each main lobe in $I'_{OCT}(n)$.

5-3. Calculate the position error Δz_0 using Eq. 9.

5-4. Calculate the corrected peaks $P_{new}(l)$ for each main lobe using Eq. 10.

5-5. Obtain the new A-scan data $I''_{OCT}(n)$ which have the new peaks $P_{new}(l)$ instead of $P(l)$.

Step 6. Map the new A-scan data $I''_{OCT}(n)$ to the grayscale data $G(n)$ using logarithm function.

Step 7. Repeat the above from Step 2 until obtaining M rows of the grayscale data $G(n)$ to obtain a frame image of SD-OCT, where M is the A-scan number of one frame image.

Step 8. Repeat the above from Step 2 until obtaining all the OCT images and display the OCT images.

1.2 Experimental Methods

The schematic of SD-OCT is shown as Fig. 2. A low coherence light source is guided through the single-mode fibers (SMF). A fiber coupler (FC) is used to couple and split the light rays. Lenses (L2, L3) are used to focus the light rays, and lenses (L1, L3, L5) are used to collimate the light rays. A polarization controller (PC) is used to control the intensity of the coherence. A galvo scanner (GS) is used to control scanned area. The spectrometer is composed of a transmission grating (G) and a line scan camera connected to a computer workstation (CW) though a cam-link cable. The CW is responsible for the data processing and controls the line scan camera for imaging and the GS to scan the entire tissue region. We use the same component as in Ref. [28]. There is no new hardware used in this SD-OCT system, and the method proposed in this paper is compatible with current other OCT imaging devices.

To demonstrate the potential of the method proposed for visualizing subcellular and extracellular microstructures with enhanced sensitivity and better definition, an optical wedge, freshly excised eyes from rat and fixed human aortic tissues were utilized. We compared the results of our method with those of the conventional FFT method[28], histogram matching[18] and the spectral shaping method[26]. CNRs of these OCT images obtained using the above-mention existing methods were calculated, and the ability to resolve Descemet's membrane and endothelium was also tested.

At the same time, we tested the average calculation time of

different methods on the same data with a computer workstation (DELL PRECISION M6800 i7-4810MQ CPU @2.8 GHz, 16 GB RAM). We also tested the performance of different methods under different Gaussian noise levels by numerical simulation by increasing the power of the Gaussian noise added to the same interferograms.

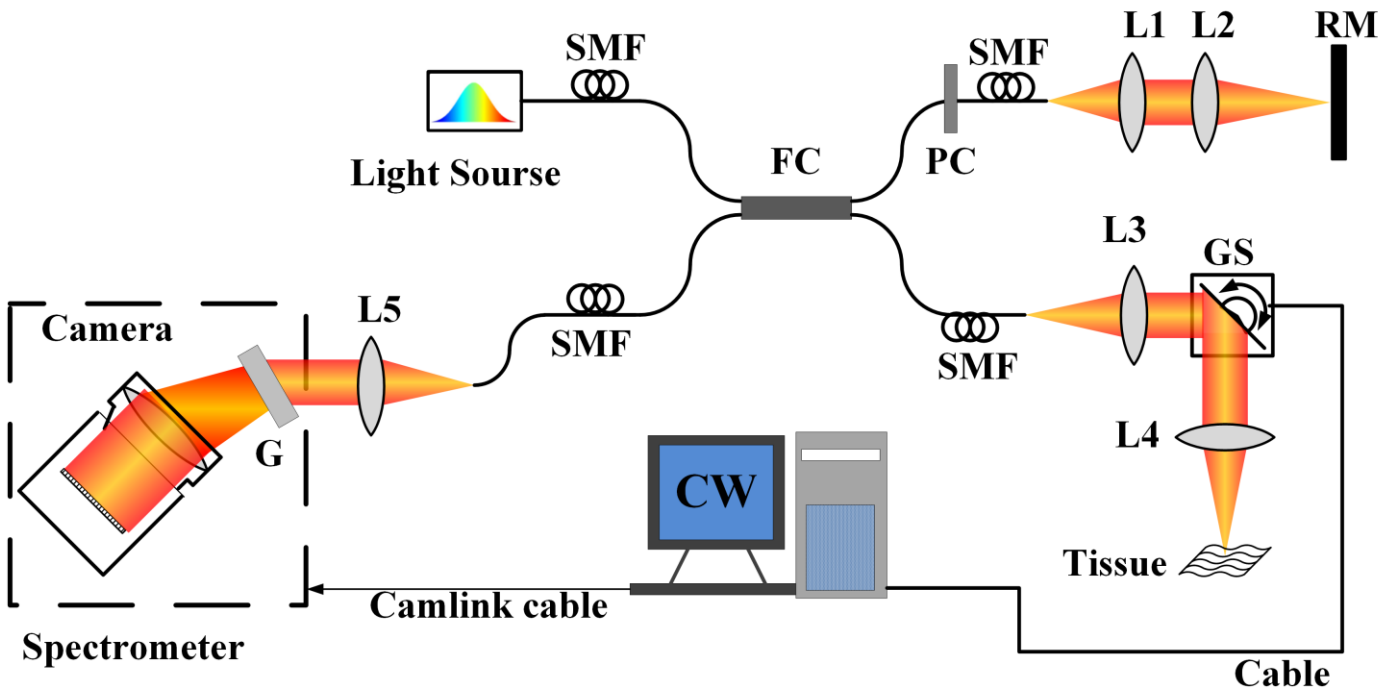

Fig. 2. Schematic of SD-OCT, SMF: single mode fiber; FC: fiber coupler; PC: polarization controller; GS: galvo scanner; G: grating; L1-L6: lens; RM: reference mirror; CW: computer workstation.

2. Results

Fig. 3, Fig. 4 and Fig. 5 show OCT images of the optical wedge, fixed human aortic tissues and freshly excised eyes from rat, respectively. Fig. 6 shows the ability of different methods to resolve corneal Descemet's membrane and endothelium. Fig. 7 shows the performance of different methods under different noise levels compared with the power of the background in the original data. Table I shows CNRs of OCT images obtained using different methods calculated using the same computational formula as in Ref. [18]. Table II shows the calculation time of different methods when dealing with the same dataset.

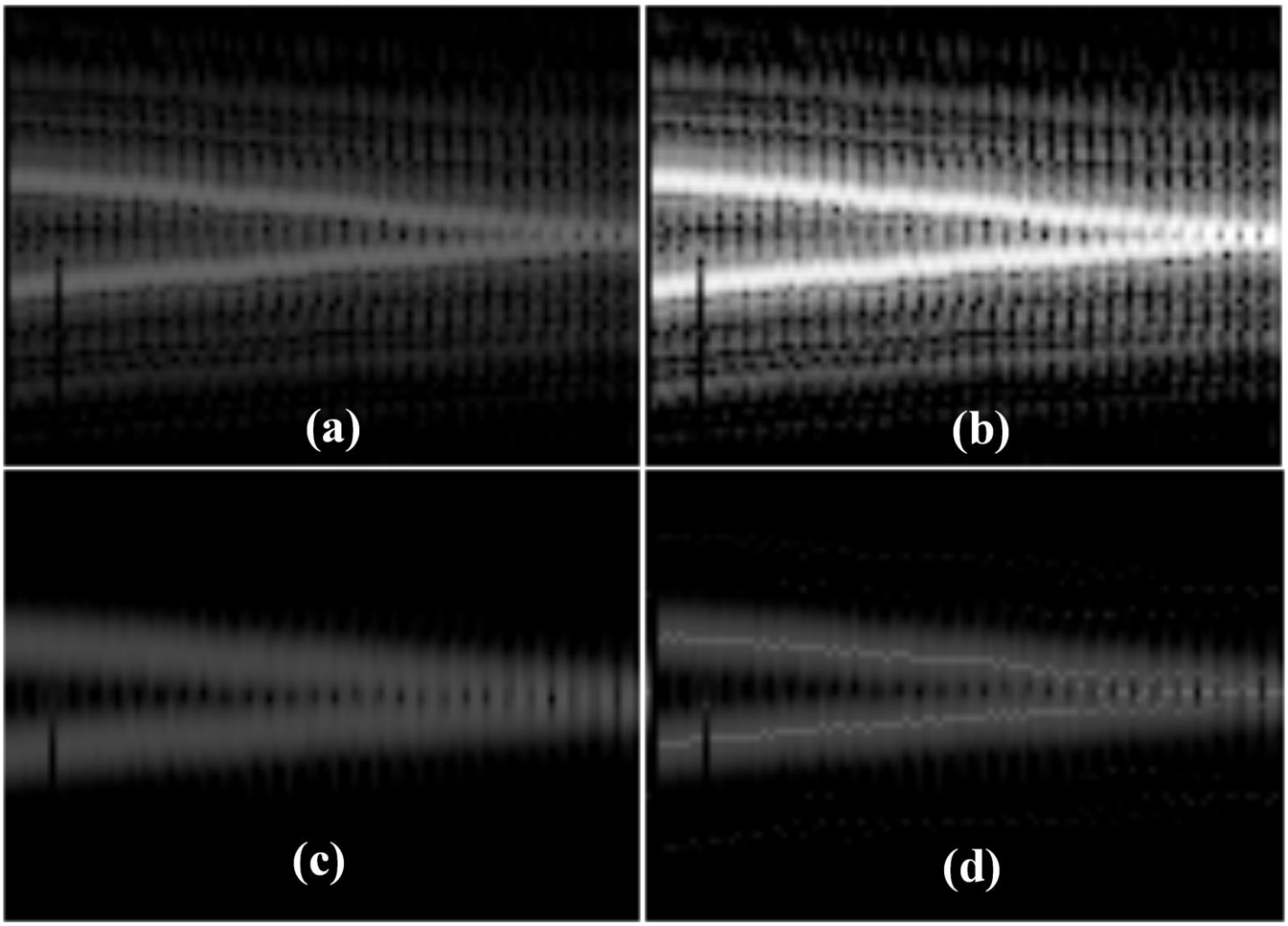

Fig. 3. OCT images of the optical wedge obtained using different methods. (a) Images obtained using the conventional FFT method; (b) images obtained using histogram matching; (c) images obtained using the spectral shaping method; (d) images obtained using the spectrum correction proposed in this paper.

Table I

CNRs of images obtained using different methods.

Methods	CNRs of Fig. 4 (dB)	CNRs of Fig. 5 (dB)
Conventional FFT method	1.0380	4.5084
Histogram matching	1.2385	4.9886
The spectral shaping method	0.7815	4.1084
The proposed method here	4.2975	5.9863

Table II

Calculation time of different methods.

Methods	Total Frames	Total Time(S)	Average Time(S)
Conventional FFT method	1023	229.011053	0.223862
Histogram matching	1023	385.806036	0.377132
The spectral shaping method	1023	502.656330	0.491355
The proposed method here	1023	2933.316241	2.867366

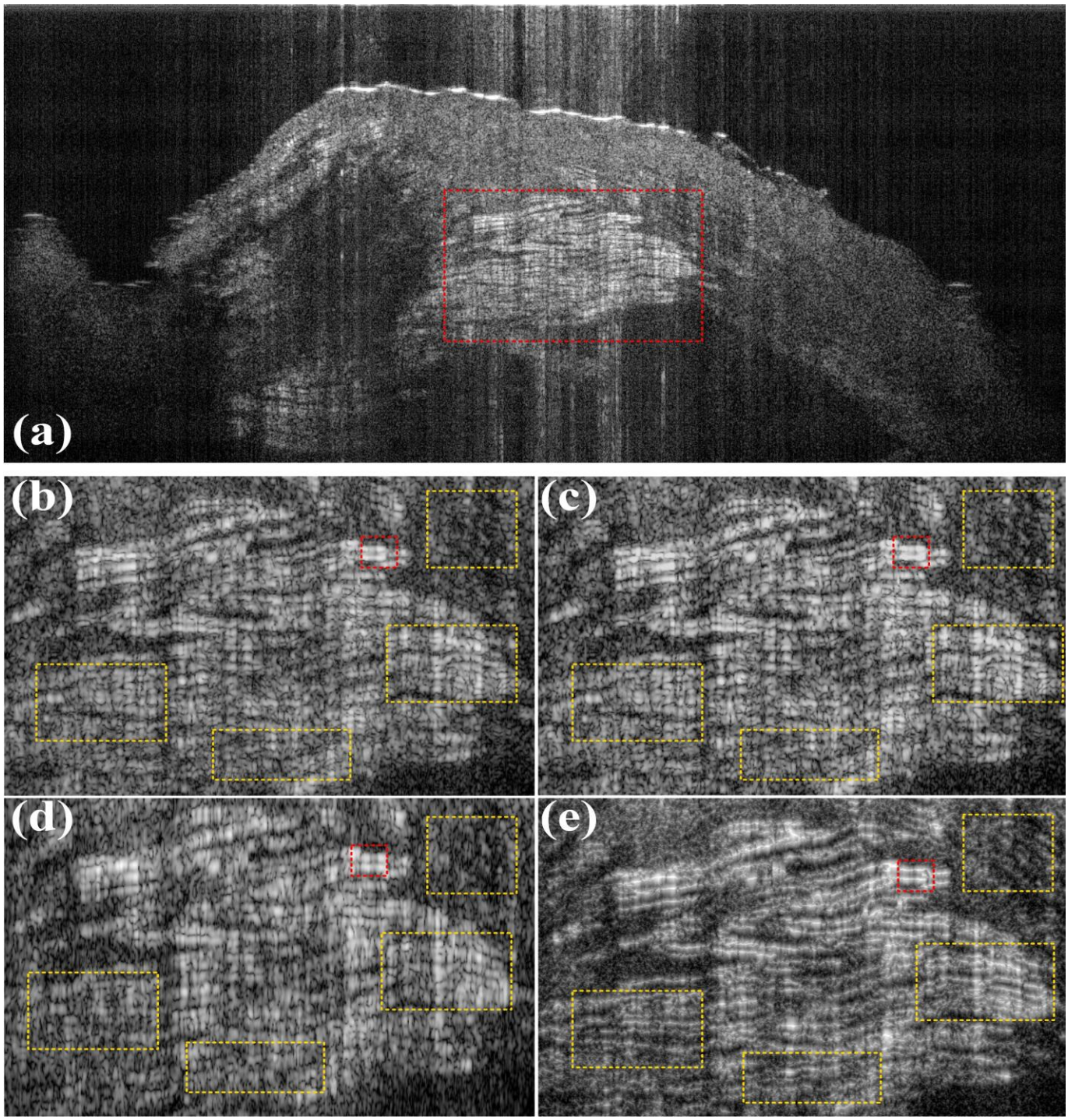

Fig. 4. OCT images of human atherosclerotic plaque. (a) A full image using the conventional FFT method; (b) a part of OCT image of (a); (c) the same part of the SD-OCT image obtained using histogram matching; (d) the same part of the SD-OCT image obtained using the spectral shaping method; (e) the same part of the SD-OCT image obtained using spectrum correction method proposed in this paper.

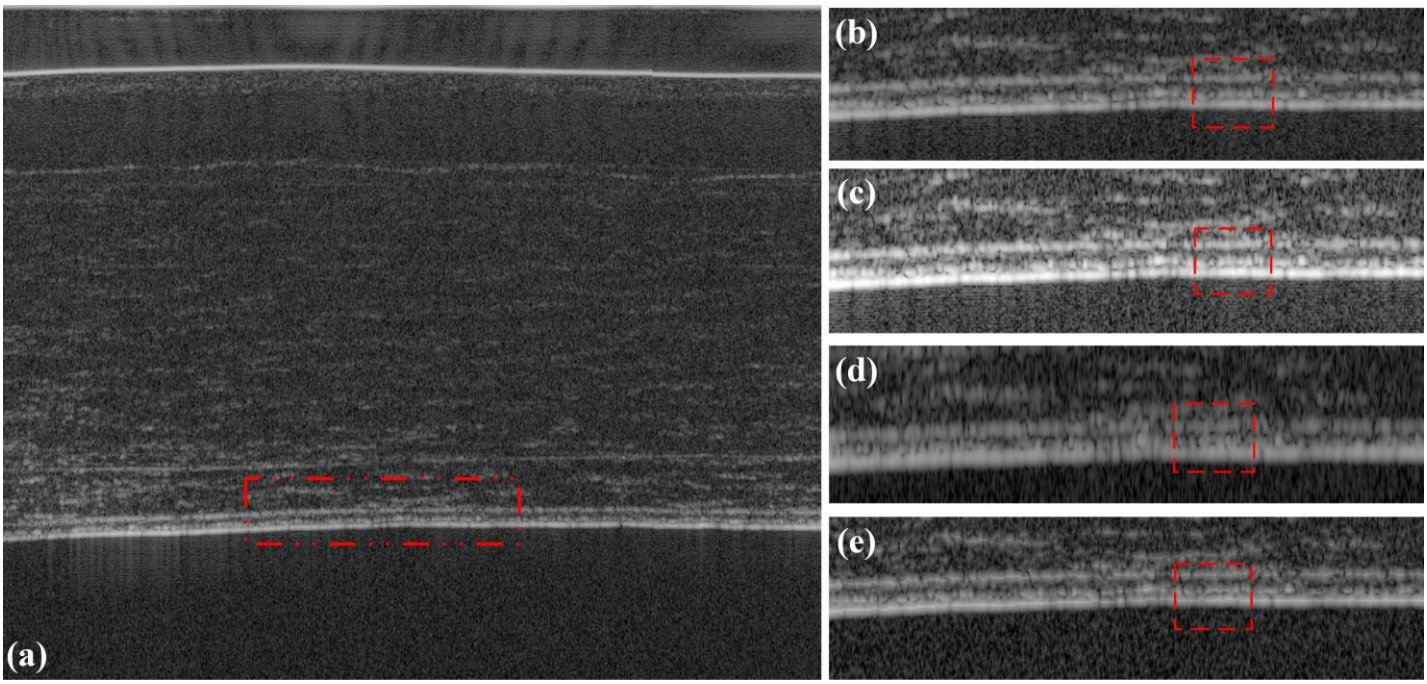

Fig. 5. OCT images of rat cornea. (a) A full image using the conventional FFT method; (b) A part of the SD-OCT image of (a); (c) the same part of the SD-OCT image obtained using histogram matching; (d) the same part of the SD-OCT image obtained using the spectral shaping method; (e) the same part of the SD-OCT image obtained using the spectrum correction method proposed in this paper.

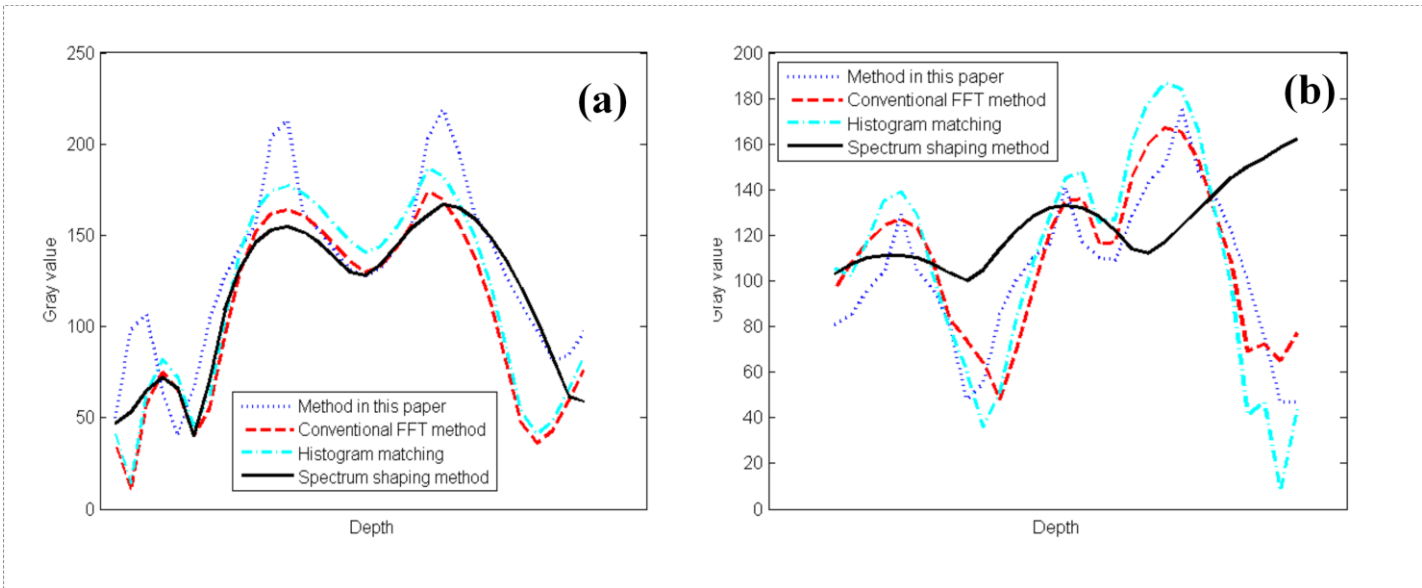

Fig. 6. Comparison of the ability to resolve Descemet's membrane and endothelium between different methods. (a) Comparison between different methods in the same region (in the small red box) in Fig. 4. (b) Comparison between different methods in the same region (in the small red box) in Fig. 5.

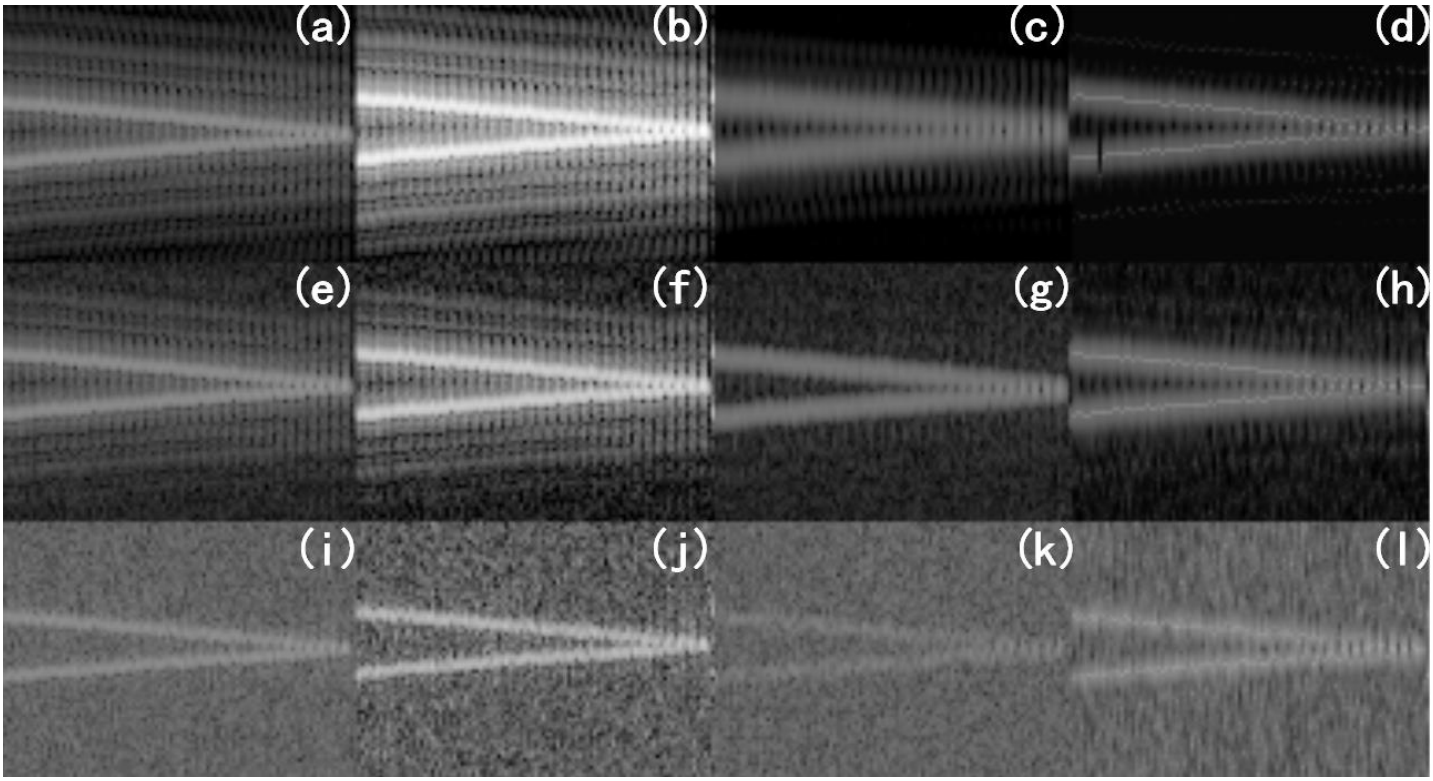

Fig. 7. Performance of different methods under different noise levels compared with the power of the light source. (a), (e) and (i) are OCT images obtained using the conventional FFT method under Gaussian noise levels of -70 dB, -50 dB and -30 dB; (b), (f), and (j) are OCT images obtained using histogram matching under Gaussian noise levels of --70 dB, -50 dB and -30 dB; (c), (g) and (k) are OCT images obtained using the spectral shaping method under Gaussian noise levels of -70 dB, -50 dB and -30 dB; and (d), (h) and (l) are OCT images obtained using the spectrum correction method proposed in this paper under Gaussian noise levels of -70 dB, -50 dB and -30 dB.

Fig. 3(a) shows that the image of conventional FFT method has serious sidelobe artifacts, which degrades image contrast. Fig. 3(b) shows the image contrast has been improved, but the sidelobe artifacts are also enhanced. Fig. 3(c) shows that although the sidelobe artifacts are suppressed by the spectral shaping method, the resolution and contrast are reduced, which makes it difficult to observe the details of the tissue microstructure. Fig. 3(d) shows that our method using spectrum correction suppresses the sidelobe artifacts and enhances the SD-OCT image contrast.

In Fig. 4(a) and Fig. 4(b), it is difficult to observe the detailed cardiovascular microstructure, such as the upper and lower surfaces of cholesterol crystals. Fig. 5(a) shows that the image acquired by the conventional FFT method has serious sidelobe artifacts, which degrade the image contrast. It is difficult to observe the detailed cornea microstructure in Fig. 5(b) because the image acquired by the conventional FFT method has serious sidelobe artifacts. Fig. 4(c) and Fig. 5(c) show that although histogram matching provides a better image contrast, the images still suffer from sidelobe artifacts. Fig. 4(d) and Fig. 5(d) show that although the spectral shaping method suppresses the sidelobe artifacts, it reduces the resolution and contrast at the mean time, which makes it difficult to observe the detailed tissue microstructure. Fig. 4(e) and Fig. 5(e) show

that the method proposed in this paper suppresses sidelobe artifacts and enhances the SD-OCT image contrast, which makes it easier to observe the microstructure of human vascular tissue and rat cornea. From Table I, we can observe that Our method provides improved CNRs than the conventional method by 1.4779 dB and 3.2595 dB for rat corneal tissues and human aortic tissues, respectively.

3. Discussions

From experimental results acquired from fresh rat corneas and fixed human aortic atherosclerosis tissues, as shown in Fig. 4, Fig. 5, Fig. 6 and Table I, we can observe that the proposed method using spectrum correction enhances SD-OCT image contrast and provides clearer microstructural information than the conventional FFT method[28], histogram matching[18] and the spectral shaping method[26]. However, Table II shows that the conventional FFT method has an advantage on calculation time compared to the other three methods, whereas our proposed method requires highest computational cost. Our current processing algorithm is suboptimal due to its serial processing fashion, so the computational speed of our proposed method can be eventually improved using parallel computing.

The tissue structures we used for our experimental verifications were all highly reflective or scattering ones. To characterize the performance of our method at various SNR levels, we numerically added Gaussian noise to the optical wedge data and compare the imaging contrast qualitatively. As shown in Fig. 7, the proposed method has good and steady performance under different Gaussian noise levels compared to other methods. However, the proposed method still requires an adequate SNR of 10 dB to achieve the optimal performance as the process of magnitude estimate is subject to noise.

4. Conclusion

In this work, we addressed a fundamental problem of sub-optical contrast and resolution in SD-OCT images, which has not been properly addressed by previous methods. We demonstrated the theoretical framework of our solutions in detail and tested the feasibility of the proposed method using a simple phantom and complex biological tissues. The results demonstrate a clear advantage in imaging contrast over the existing methods.

In conclusion, we developed a digital signal processing method to enhance SD-OCT image contrast. The proposed spectrum correction method suppressed sidelobe artifacts and strengthened the coherence numerical value in the main lobe of the axial point function to enhance SD-OCT image contrast. Experimental results on fresh and fixed tissues confirmed the effectiveness of this method and agreed well with our theoretical predictions. We further noted that this method works best under the condition of sufficient signal to noise ratio, and will be very useful in detecting highly reflective tissue microstructures such as corneal endothelium, cholesterol crystals in atherosclerotic plaques, and stent polymers.

Funding

This research was supported in part by the National Natural Science Foundation of China (Grant No. 61705184), the National Research Foundation Singapore (NRF-CRP13-2014-05), Ministry of Education Singapore (MOE2013-T2-2-107), National Medical Research Council Singapore (NMRC/CBRG/0036 /2013) and NTU-AIT-MUV program in advanced biomedical imaging (NAM/15005).

Acknowledgements

The authors thank all the members of the Fiber Technology Lab at Nanyang Technological University and professor Yutang Ye from the University of Electronic Science and Technology of China for their valuable support for this work.

References

[1] M. Adhi and J. S. Duker, "Optical coherence tomography–current and future applications," *Current opinion in ophthalmology,* vol. 24, p. 213, 2013.

[2] D. C. Adler, Y. Chen, R. Huber, J. Schmitt, J. Connolly, and J. G. Fujimoto, "Three-dimensional endomicroscopy using optical coherence tomography," *Nature Photonics,* vol. 1, pp. 709-716,

2007.

[3] D. Huang, E. A. Swanson, C. P. Lin, J. S. Schuman, W. G. Stinson, W. Chang*, et al.*, "Optical coherence tomography," *Science (New York, NY),* vol. 254, p. 1178, 1991.

[4] J. G. Fujimoto, "Optical coherence tomography for ultrahigh resolution in vivo imaging," *Nature biotechnology,* vol. 21, pp. 1361-1367, 2003.

[5] L. Liu, K. K. Chu, G. H. Houser, B. J. Diephuis, Y. Li, E. J. Wilsterman*, et al.*, "Method for quantitative study of airway functional microanatomy using micro-optical coherence tomography," *PloS one,* vol. 8, p. e54473, 2013.

[6] L. Liu, J. A. Gardecki, S. K. Nadkarni, J. D. Toussaint, Y. Yagi, B. E. Bouma*, et al.*, "Imaging the subcellular structure of human coronary atherosclerosis using micro-optical coherence tomography," *Nature medicine,* vol. 17, pp. 1010-1014, 2011.

[7] L. Liu, S. Shastry, S. Byan-Parker, G. Houser, K. K. Chu, S. E. Birket*, et al.*, "An autoregulatory mechanism governing mucociliary transport is sensitive to mucus load," *American journal of respiratory cell and molecular biology,* vol. 51, pp. 485-493, 2014.

[8] W. Drexler, M. Liu, A. Kumar, T. Kamali, A. Unterhuber, and R. A. Leitgeb, "Optical coherence tomography today: speed, contrast, and multimodality," *Journal of biomedical optics,* vol. 19, pp. 071412-071412, 2014.

[9] J. Holmes and J. Welzel, "OCT in Dermatology," *Optical Coherence Tomography: Technology and Applications,* pp. 2189-2207, 2015.

[10] M. Kashiwagi, L. Liu, K. K. Chu, C.-H. Sun, A. Tanaka, J. A. Gardecki*, et al.*, "Feasibility of the assessment of cholesterol crystals in human macrophages using micro optical coherence tomography," *PloS one,* vol. 9, p. e102669, 2014.

[11] J. C. Kah, M. Olivo, T. H. Chow, K. S. Song, K. Z. Koh, S. Mhaisalkar*, et al.*, "Control of optical contrast using gold nanoshells for optical coherence tomography imaging of mouse xenograft tumor model in vivo," *Journal of Biomedical Optics,* vol. 14, p. 054015, 2009.

[12] T. M. Lee, A. L. Oldenburg, S. Sitafalwalla, D. L. Marks, W. Luo, F. J. Toublan*, et al.*, "Engineered microsphere contrast agents for optical coherence tomography," *Optics Letters,* vol. 28, pp. 1546-8, 2003.

[13] J. L. Pichardo-Molina and D. Luna-Moreno, "Contrast enhancement of optical coherence tomography images using branched gold nanoparticles," *Journal of Nanomaterials,* vol. 2012, p. 128, 2012.

[14] T. S. Troutman, J. K. Barton, and M. Romanowski, "Optical coherence tomography with plasmon resonant nanorods of gold," *Optics Letters,* vol. 32, pp. 1438-40, 2007.

[15] E. V. Zagaynova, M. V. Shirmanova, M. Y. Kirillin, B. N. Khlebtsov, A. G. Orlova, I. V. Balalaeva*, et al.*, "Contrasting properties of gold nanoparticles for optical coherence tomography: phantom, in vivo studies and Monte Carlo simulation," *Physics in Medicine & Biology,* vol. 53, p. 4995, 2008.

[16] D. C. Adler, T. H. Ko, P. R. Herz, and J. G. Fujimoto, "Optical coherence tomography contrast enhancement using spectroscopic analysis with spectral autocorrelation," *Optics express,* vol. 12, pp. 5487-5501, 2004.

[17] A. Z and R. H, "Statistical Modeling of Retinal Optical Coherent Tomography," *IEEE Transactions on Medical Imaging,* vol. 35, pp. 1544-1554, 2016.

[18] Y. Liu, Y. Liang, Z. Tong, X. Zhu, and G. Mu, "Contrast enhancement of optical coherence tomography images using least squares fitting and histogram matching," *Optics Communications,* vol. 279, pp. 23-26, 2007.

[19] A. Sakamoto, M. Hangai, and N. Yoshimura, "Spectral-domain optical coherence tomography with multiple B-scan averaging for enhanced imaging of retinal diseases," *Ophthalmology,* vol. 115, pp. 1071-1078, 2008.

[20] P. Duraisamy, A. Ei-Saba, X. Yuan, and B. Giri, "Visual contrast enhancement of optical coherence tomography images by combined and image fusion methods," in *International Conference on Computing Communication and NETWORKING Technologies*, 2010, pp. 1-1.

[21] N. Strouthidis, J. M. Mari, S. C. Park, and M. Girard, "Enhancement of Lamina Cribrosa Visibility in Optical Coherence Tomography Images using Adaptive Compensation," *Investigative Ophthalmology & Visual Science,* vol. 54, pp. 2149-2149, 2013.

[22] M. J. Girard, N. G. Strouthidis, C. R. Ethier, and J. M. Mari, "Shadow removal and contrast enhancement in optical coherence tomography images of the human optic nerve head," *Investigative Ophthalmology & Visual Science,* vol. 52, pp. 7738-48, 2011.

[23] D. Cui, X. Liu, P. Shum, X. Yu, and L. Liu, "Micro-optical coherence tomography (μOCT) in vivo," in *Imaging Systems and Applications*, 2014, p. IM3C. 5.

[24] D. Cui, X. Liu, J. Zhang, X. Yu, S. Ding, Y. Luo*, et al.*, "Dual spectrometer system with spectral compounding for 1- μ m optical coherence tomography in vivo," *Optics letters,* vol. 39, pp. 6727-6730, 2014.

[25] X. Yu, X. Liu, S. Chen, Y. Luo, X. Wang, and L. Liu, "High-resolution extended source optical coherence tomography," *Optics express,* vol. 23, pp. 26399-26413, 2015.

[26] R. Tripathi, N. Nassif, J. S. Nelson, B. H. Park, and J. F. de Boer, "Spectral shaping for non-Gaussian source spectra in optical coherence tomography," *Optics Letters,* vol. 27, pp. 406-408, 2002.

[27] X. Ming and D. Kang, "Corrections for frequency, amplitude and phase in a fast Fourier transform of a harmonic signal," *Mechanical Systems and Signal Processing,* vol. 10, pp. 211-221, 1996.

[28] X. Yu, Y. Luo, X. Liu, S. Chen, X. Wang, S. Chen*, et al.*, "Toward High-Speed Imaging of Cellular Structures in Rat Colon Using Micro-optical Coherence Tomography," *IEEE Photonics Journal,* vol. 8, pp. 1-8, 2016.